

---

# Physics of nova outbursts: A theoretical model of classical nova outbursts with self-consistent wind mass loss

Mariko KATO<sup>1</sup>, Hideyuki SAIO,<sup>2</sup> and Izumi HACHISU<sup>3</sup>

<sup>1</sup>Department of Astronomy, Keio University, Hiyoshi, Yokohama 223-8521, Japan

<sup>2</sup>Astronomical Institute, Graduate School of Science, Tohoku University, Sendai, 980-8578, Japan

<sup>3</sup>Department of Earth Science and Astronomy, College of Arts and Sciences, The University of Tokyo, 3-8-1 Komaba, Meguro-ku, Tokyo 153-8902, Japan

\*E-mail: mariko.kato@hc.st.keio.ac.jp

Received 2021 December 8; Accepted 2022 June 7

## Abstract

We present a model for one cycle of a classical nova outburst based on a self-consistent wind mass loss accelerated by the gradient of radiation pressure, i.e., the so-called optically thick winds. Evolution models are calculated by a Henyey code for a  $1.0 M_{\odot}$  white dwarf (WD) with a mass accretion rate of  $5 \times 10^{-9} M_{\odot} \text{ yr}^{-1}$ . The outermost part of hydrogen-rich envelope is connected to a steadily moving envelope when optically thick winds occur. We confirm that no internal shock waves occur at the thermonuclear runaway. The wind mass loss rate reaches a peak of  $1.4 \times 10^{-4} M_{\odot} \text{ yr}^{-1}$  at the epoch of the maximum photospheric expansion, where the photospheric temperature decreases to  $\log T_{\text{ph}} \text{ (K)}=3.90$ . Almost all of the accreted mass is lost in the wind. The nuclear energy generated in hydrogen burning is lost in a form of photon emission (64 %), gravitational energy (lifting-up the wind matter against the gravity, 35 %), and kinetic energy of the wind (0.23 %). A classical nova should be very bright in a far-UV (100 - 300 Å) band, during a day just after the onset of thermonuclear runaway ( $\sim 25$  d before the optical maximum). In the decay phase of the nova outburst, the envelope structure is very close to that of a steady state solution.

**Key words:** novae, cataclysmic variables — stars: interiors — stars: mass-loss — white dwarfs — X-rays: binaries

---

## 1 Introduction

A nova is a thermonuclear runaway event on a mass-accreting white dwarf (WD) (Nariai et al. 1980; Iben 1982; Prialnik et al. 1986; Sion et al. 1979; Sparks et al. 1978). During a nova outburst the hydrogen-rich envelope expands to a giant size and wind mass loss is accelerated. Such a nova outburst has been calculated by several groups with Henyey-type evolution codes (Prialnik and Kovetz 1995; Kovetz 1998; Denissenkov et al. 2013; Idan et al.

2013; Wolf et al. 2013; Kato et al. 2014; Kato et al. 2015; Tang et al. 2014). These codes, however, encounter numerical difficulties when the nova envelope expands and wind mass loss occurs. To continue the numerical calculation beyond the extended stage, various mass loss schemes are assumed. However, some of these mass loss rates are not always consistent with the physical mechanism of wind acceleration (see Kato et al. (2017) for a review and comparison of various numerical methods).

The most important mass-loss mechanism during a

nova outburst is the wind accelerated by the radiation pressure-gradient deep inside the photosphere (Friedjung 1966; Finzi & Wolf 1971; Zytkov 1972; Ruggles & Bath 1979). Massive winds occur when the envelope expands and hence the temperature in the envelope decreases to the range where the radiative opacity increases outward (Kato 1983; Kato 1985; Kato 1997; Kato and Hachisu 1994; Kato and Hachisu 2009a). Once the optically thick winds occur, other acceleration mechanisms such as a line-driven wind are inefficient mainly because of lack of photon momentum (see sections 5 and 6.2 in Kato and Hachisu (1994)). In order to follow the decay phase of nova outbursts Kato (1983) and Kato and Hachisu (1994) developed the optically thick wind theory assuming that the envelope has settled to a steady state and thermal equilibrium. A sequence of steady state solutions can successfully follow the evolution of a nova and reproduce its multiwavelength light curves in the decline phase.

The optically thick wind theory, however, cannot be applied to the rising phase of a nova outburst because the expanding envelope has not yet reached the steady state. In order to follow a cycle of nova evolution, it is necessary to incorporate optically thick winds into evolution calculations. Recently, Kato et al. (2017a) succeeded in calculating multi cycles of *recurrent* nova evolutions with a Henyey-type code including the optically thick winds. Their models are for two cases of recurrent novae, i.e.,  $1.2 M_{\odot}$  WD and  $1.38 M_{\odot}$  WD with the mass accretion rates of  $2.0 \times 10^{-7} M_{\odot} \text{ yr}^{-1}$  and  $1.6 \times 10^{-7} M_{\odot} \text{ yr}^{-1}$ , respectively. The hydrogen shell flashes in these recurrent novae are weaker compared with those in classical novae with smaller accretion rates.

In this paper we obtain evolution models of a *classical* nova cycle. The thermonuclear runaway in a classical nova is much stronger, because the hydrogen-rich envelope accumulated before the ignition is more massive so that the envelope expands to a giant size. For this reason, modeling the evolution of a classical nova cycle is more demanding than the case of recurrent novae. We have calculated  $1.0 M_{\odot}$  WD evolution models for one cycle of a classical nova outburst, assuming a quiescent accretion rate of  $5 \times 10^{-9} M_{\odot} \text{ yr}^{-1}$ . Mass loss rates in expanded phases are set to be consistent with the optically thick wind model. We present the temporal change of internal structure of the envelope, occurrence of the wind mass loss, energy balance of mass-losing envelope, and ejecta mass etc. We also compare our results with multiwavelength light curves obtained by Hillman et al. (2014) based on the hydrogen shell flash models in Prialnik and Kovetz (1995) and Yaron et al. (2005).

Because in this work we assume spherical symmetry,

non-spherical phenomena are not included. Our model also doesn't include physical processes that occur outside the photosphere, e.g., free-free emission from ejecta (Hachisu and Kato 2015), dust formation (e.g., OS And: Kikuchi et al. (1988), V2362 Cyg Arai et al. (2010), FH Ser: Gehrz et al. (1988)), shock wave when the ejecta collide with circumbinary matter and associated phenomena like heating, gamma ray emission, etc. (Aydi et al. 2020; Chomiuk et al. 2021; Drake and Orland 2010; H.E.S.S. 2022).

This paper is organized as follows. Section 2 describes our calculation method. Our numerical results are presented separately, for one cycle of a nova outburst evolution in section 3, temporal changes of internal structures in section 4, energy budget in section 5, and UV/X-ray flashes in section 6. Discussion and conclusions follow in sections 7 and 8, respectively.

## 2 Numerical method

We have calculated multicycle nova evolution of a  $1.0 M_{\odot}$  white dwarf (WD) accreting matter at a rate of  $5 \times 10^{-9} M_{\odot} \text{ yr}^{-1}$ . We adopt this mass accretion rate as a central value of the distribution of mass accretion rates from Selvelli & Gilmozzi (2019)'s Figure 3. Their median value is about  $3 \times 10^{-9} M_{\odot} \text{ yr}^{-1}$ , which is close to our adopted value. The chemical compositions of the accreting matter and initial hydrogen-rich envelope of the WD are assumed to be  $X = 0.7$ ,  $Y = 0.28$ , and  $Z = 0.02$ . We assume that the CO core is composed of 48% of  $^{12}\text{C}$ , 50% of  $^{16}\text{O}$ , and 2% of  $^{20}\text{Ne}$  by weight. This assumption does not affect our results because the CO core material hardly mixes with the upper part and the newly accreted matter is burned into heavy elements and accumulates on the surface of CO core. We used the same computer code with the OPAL opacity tables (Iglesias and Rogers 1996) as those used in our models of recurrent novae published in Kato et al. (2017a); Kato et al. (2017b); Kato et al. (2018), in which more details of the method of calculations and input physics are discussed (e.g., the number of meshes, numerical convergence, equations of state, and nuclear burning networks).

For the initial WD model of our evolution calculations, we adopted a steady-state equilibrium model (Kato et al. 2014), in which the heating by the mass accretion and nuclear energy generation is balanced with the cooling by radiative diffusion and neutrino emission. The model has parameters of  $\log L/L_{\odot} = 2.567$ ,  $\log T_c \text{ (K)} = 7.687$ , and  $\log T_{\text{ph}} \text{ (K)} = 5.422$ . Starting from the steady-state model, the flash properties reach a limit cycle before 5th flash cycle, which indicates that the interior structure of our initial

model is already a good approximation to the structure realized after many flashes. Note that our initial WD temperature  $T_c$  is higher than that ( $< 10^7$  K) of the equilibrium core temperature of Townsley and Bildsten (2004).

The equilibrium  $1.0 M_\odot$  WD model at  $\dot{M} = 5 \times 10^{-9} M_\odot \text{yr}^{-1}$  is thermally unstable. Once we start the evolution with mass accretion, the hydrogen shell burning weakens and the luminosity begins to decrease. Meanwhile, a hydrogen-rich envelope accumulates. When the mass of hydrogen-rich envelope becomes large enough (i.e. larger than the ignition mass  $M_{\text{ig}}$ ), the nuclear burning is re-ignited at the bottom of the envelope, and the envelope expands exceeding the equilibrium radius; i.e., a hydrogen shell flash occurs. When the radius becomes very large (the radiation pressure becomes much larger than the gas pressure), the evolution calculation by our evolution code based on the Henyey method fails. Then, we assume the mass loss at a rate according to the prescription given in Kato et al. (2017a). After a certain amount of mass is lost, the envelope begins to contract. The mass loss is stopped when the radius becomes small enough (Kato et al. 2017a).

For each stage with mass loss, we calculated steady-state wind solutions with a different set of parameters (photospheric temperature, luminosity, and mass). The mass-loss rate of the wind solution is automatically determined from the boundary condition of the wind (Kato and Hachisu 1994). If the wind mass-loss rate of steady-state solution does not match to the temporarily assumed value for the Henyey code, we recalculate the nova evolution with different temporal mass-loss rates.

Figure 1 shows two mass loss rates, one is the mass loss rate initially assumed in our Henyey code and the other is the wind mass loss rate finally obtained after fitting with the optically thick wind solutions. These two mass loss rates are in good agreement with each other, suggesting that the physical properties of our wind solutions are reasonable (see also Kato et al. (2017a)). We need many iterations until we obtain mass loss rate assumed for the evolution model sufficiently close to the resultant wind mass-loss rate as described in Kato et al. (2017a).

The model parameters are summarized in Table 1. We adopt a  $1.0 M_\odot$  WD and the mass accretion rate of  $\dot{M}_{\text{acc}} = 5 \times 10^{-9} M_\odot \text{yr}^{-1}$ . We adopt this mass accretion rate as a central value of the distribution of mass accretion rates obtained by Selvelli & Gilmozzi (2019) as already mentioned in section 1 (see also, e.g., Figure 6 in Hachisu et al. (2020)). The recurrence period is 5370 years. We assume that the WD interior structure has already reached thermal equilibrium, so that its central temperature  $T_{\text{WD}}$  is not a free parameter (Kato et

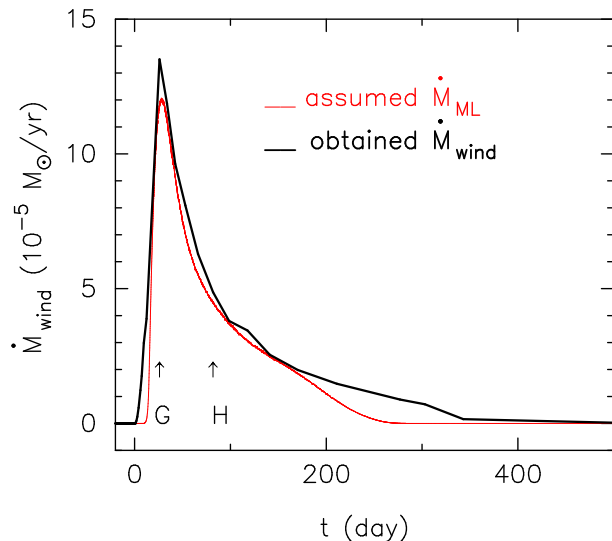


Fig. 1. Comparison of the temporarily assumed mass loss rates (thin red line) with the obtained wind mass loss rates (thick black line) after fitting.

al. 2021). The other quantities shown in Table 1 are the mass accreted in the quiescent phase  $M_{\text{acc}}$ , the ignition mass  $M_{\text{ig}}$ , the maximum temperature in the hydrogen nuclear burning layer through a flash, and the maximum value of nuclear luminosity. The difference between the accreted mass,  $M_{\text{acc}} = 2.68 \times 10^{-5} M_\odot$ , and the ignition mass,  $M_{\text{ig}} = 3.05 \times 10^{-5} M_\odot$ , corresponds to the leftover from the previous outburst; When the latest outburst ends, the hydrogen-rich envelope of  $0.37 \times 10^{-5} M_\odot$  remains on the WD. The mass accretion restarts and hydrogen-rich matter accumulates on it.

We do not include mixing processes between the core and envelope prior to the shell flash, or multi-dimensional mixing (Casanova et al. 2010; Glasner et al. 2012; José et al. 2020), to avoid free parameters of its efficiency and to simplify our calculations. After the onset of thermonuclear runaway, an extensive convection zone appears and the processed helium is carried upward to reduce the hydrogen content  $X$  in the envelope, from 0.7 to 0.65, whereas heavy element content  $Z = 0.02$  is unchanged. Effects of these simplification are discussed in subsection 7.2.

### 3 One cycle of shell flashes

#### 3.1 H-R diagram

Figure 2 shows the evolutionary track in the H-R diagram for one cycle of a classical nova outburst. In the quiescent phase the accreting WD stays around the bottom of the line (denoted by label A). After the thermonuclear runaway sets in, the luminosity increases with keeping the photospheric radius almost constant. We define the onset of the shell flash at the time when  $L_{\text{nuc}}$  reaches max-

**Table 1.** Characteristic properties of a shell flash model

$M_{\text{WD}}$ ( $M_{\odot}$ )	$\dot{M}_{\text{acc}}$ ( $M_{\odot} \text{ yr}^{-1}$ )	$\log T_{\text{WD}}$ (K)	$P_{\text{rec}}$ (yr)	$M_{\text{acc}}$ ( $M_{\odot}$ )	$M_{\text{ig}}$ ( $M_{\odot}$ )	$\log T^{\text{max}}$ (K)	$\log L_{\text{nuc}}^{\text{max}}$ ( $L_{\odot}$ )
1.0	$5 \times 10^{-9}$	7.687	5370	$2.68 \times 10^{-5}$	$3.04 \times 10^{-5}$	8.18	8.36

**Table 2.** Time since the beginning of the flash

Stage	B	C	D	E	F	G	H	I	J
	$L_{\text{nuc}}^{\text{max}}$	$T_{\text{ph}}^{\text{max}}$	X flash	wind starts		max exp		wind ends	$0.1 L_{\text{X}}^{\text{max}}$
Time (day)	0.0	0.063	0.114	1.05	2.83	26.0	81.9	530	6.46 yr
$\log T_{\text{ph}}$ (K)	5.102	5.577	5.568	5.319	5.006	3.900	4.305	5.427	5.676
$\dot{M}_{\text{wind}}$ ( $10^{-5} M_{\odot} \text{ yr}^{-1}$ )	-	-	-	0.0	0.25	13.5	4.9	0.0	-

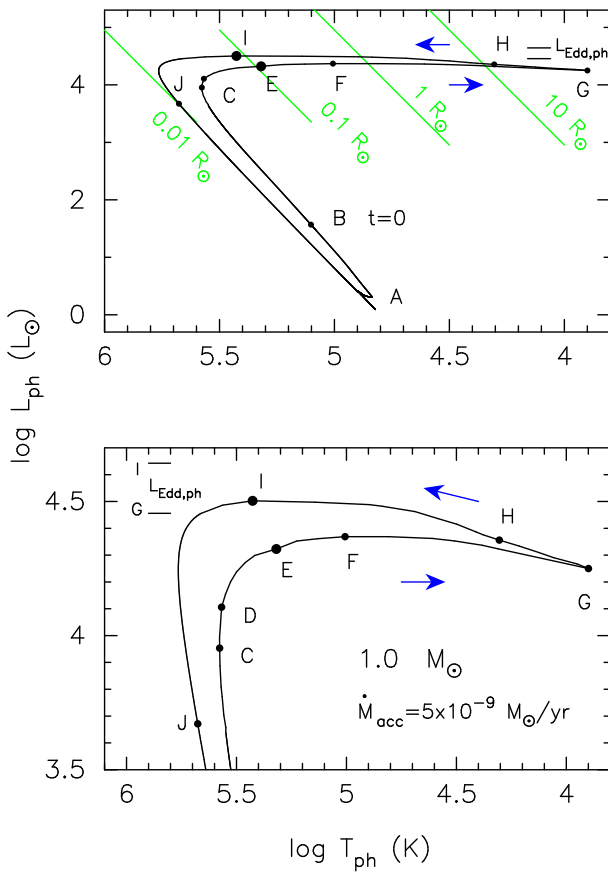


**Fig. 2.** The H-R diagram of a shell flash on a  $1.0 M_{\odot}$  WD with the mass accretion rate of  $\dot{M}_{\text{acc}} = 5 \times 10^{-9} M_{\odot} \text{ yr}^{-1}$ . Lower panel is an enlargement of the top part of the upper panel. A: Quiescent phase before the shell flash. B: The epoch when  $L_{\text{nuc}}$  reaches the maximum value ( $t = 0$ ). C: The photospheric temperature takes the maximum value in the rising phase. D: X-ray flash (see section 6). E: The wind mass loss begins. F: The epoch at  $\log T_{\text{ph}} (K) = 5.0$ . G: The maximum expansion when the wind mass loss rate and photospheric radius reach maximum. H: The epoch at  $\log T_{\text{ph}} (K) = 4.3$ . I: The wind mass loss stops. J: The supersoft X-ray luminosity decreases to one tenth of the maximum value.

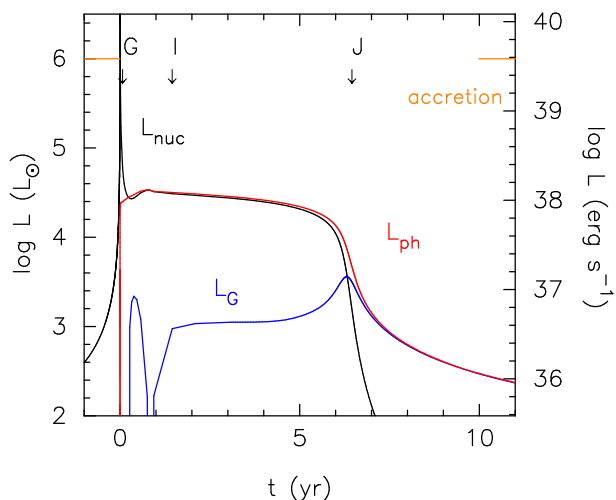
imum, the point of which is denoted by label B ( $t = 0$ ). The photospheric temperature also increases and reaches maximum  $T_{\text{ph}}^{\text{max}}$  at epoch C. Then, the envelope begins to expand, and the optically thick winds start at point E. At stage G the photospheric radius attains its maximum and the wind mass loss rate also reaches maximum. As the envelope mass decreases mainly due to wind mass loss and lesser extent by hydrogen burning, the photospheric radius decreases and the temperature  $T_{\text{ph}}$  increases with time. The winds stop at point I. After stage I the envelope mass continuously decreases owing to hydrogen burning. Epoch J is the stage when the supersoft X-ray luminosity decreases to one tenth of its maximum value (section 6). The time of each epoch is summarized in table 2.

Figure 2 also shows two local Eddington luminosities at the photosphere for two stages G and I,

$$L_{\text{Edd,ph}} \equiv \frac{4\pi c G M_{\text{WD}}}{\kappa_{\text{ph}}}, \quad (1)$$

where  $\kappa_{\text{ph}}$  is the opacity at the photosphere. At stage G,  $L_{\text{Edd,ph}} = 1.1 \times 10^{38} \text{ erg sec}^{-1} = 2.9 \times 10^4 L_{\odot}$  ( $\kappa_{\text{ph}} = 0.458$ ), while at stage I,  $L_{\text{Edd,ph}} = 1.7 \times 10^{38} \text{ erg sec}^{-1} = 4.3 \times 10^4 L_{\odot}$  ( $\kappa_{\text{ph}} = 0.301$ ). These values are indicated by the short horizontal bars in figure 2. The photospheric luminosity  $L_{\text{ph}}$  does not exceed the photospheric Eddington luminosity  $L_{\text{Edd,ph}}$ .

Observationally nova brightness often exceeds the Eddington limit ( $M_V \sim -6$ , see e.g. Hachisu and Kato (2004)). Hachisu and Kato (2006) explained that the observed brightness is owing to free-free emission originated from ejecta outside the photosphere, and not always attributed to the photospheric blackbody emission. The brightness of free-free emission in novae is mainly determined from the wind mass loss rate. When the mass loss rate is larger, the free-free emission can exceed the Eddington limit. Hachisu and his group reproduced multi-wavelength light curves of a number of novae including super Eddington phase (Hachisu and Kato (2006); Hachisu et al. (2008); Hachisu and Kato (2015); Hachisu and Kato (2016a); Hachisu & Kato (2018a); Hachisu & Kato



**Fig. 3.** The evolution of the photospheric luminosity,  $L_{\text{ph}}$ , total nuclear burning energy release rate,  $L_{\text{nuc}}$ , and total gravitational energy release rate,  $L_{\text{G}}$ . We stopped the mass accretion at  $t = 7 \times 10^{-4}$  year and restarted at  $t = 9.99$  year, the period of which is indicated with the horizontal orange line. Epoch B in Fig.2 corresponds to the time of  $t = 0$  and three epochs G (maximum photospheric expansion), I (end of winds), and J (supersoft X-ray luminosity decreases to one tenth of its maximum) are indicated by the downward arrows.

(2018b); Hachisu & Kato (2019a); Hachisu & Kato (2019b); Hachisu et al. (2020); Hachisu & Kato (2021a)). The sub-Eddington value of the photospheric luminosity does not conflict with the observational super-Eddington luminosities.

### 3.2 Energy generation in thermonuclear runaway

Figure 3 shows the evolution of the emergent bolometric luminosity  $L_{\text{ph}}$ , total nuclear energy release rate  $L_{\text{nuc}} = \int \epsilon_{\text{nuc}} \delta m$ , and integrated gravitational energy release rate  $L_{\text{G}} = \int \epsilon_{\text{g}} \delta m$ . Here,  $\epsilon_{\text{nuc}}$  and  $\epsilon_{\text{g}}$  are energy generation rates per unit mass owing to nuclear burning and gravitational energy release, respectively. We stopped the mass accretion when  $L_{\text{ph}}$  increases to  $\log L_{\text{ph}}/L_{\odot} = 3.5$  ( $\log T_{\text{ph}}$  (K) = 5.53) and resumed it when the luminosity decreases to  $\log L_{\text{ph}}/L_{\odot} = 2.48$  ( $\log T_{\text{ph}}$  (K) = 5.40). The accretion phase is indicated with the horizontal orange lines.

In the very beginning of the outburst the nuclear energy generation rate  $L_{\text{nuc}}$  is much larger than the photospheric luminosity  $L_{\text{ph}}$ . The rest energy is absorbed ( $L_{\text{G}} < 0$ ) and used to expand the envelope against the gravity. As the envelope expands,  $L_{\text{nuc}}$  decreases rapidly and becomes comparable with  $L_{\text{ph}}$  (figure 3). After that the absorbed energy is gradually released as the expanded layers slowly contracts.

Figure 4 shows a close-up view of the energy conservation during the epoch of thermonuclear runaway. The nuclear energy release rate increases in a timescale of

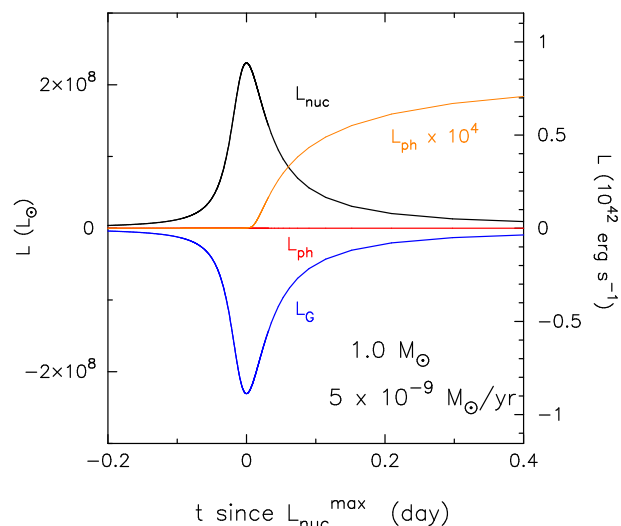


**Fig. 4.** Close-up view of a very early phase of the shell flash in figure 3. The orange line denotes  $10^4$  times the photospheric luminosity (red line),

$\sim 0.03$  day ( $\sim 2600$  sec) to reach the maximum value of  $L_{\text{nuc}}^{\text{max}} = 2.3 \times 10^8 L_{\odot}$ , while most of the released nuclear energy is absorbed (i.e.,  $L_{\text{nuc}} \sim -L_{\text{G}} \gg L_{\text{ph}}$ ) to expand the envelope.

In stage B ( $t = 0$ ) the temperature reaches  $\log T$  (K) = 8.18, where the density is  $\log \rho$  ( $\text{g}/\text{cm}^3$ ) = 2.41 and radius is  $\log R/R_{\odot} = -2.099$ . The local thermal timescale is roughly estimated to be  $(u/\epsilon_{\text{nuc}}) = 131$  sec, where  $u$  is the specific thermal energy,  $u = 4.16 \times 10^{16}$  erg  $\text{g}^{-1}$ , and  $\epsilon_{\text{nuc}}$  is the nuclear burning rate per unit mass  $\epsilon_{\text{nuc}} = 3.18 \times 10^{14}$  erg  $\text{g}^{-1} \text{sec}^{-1}$ . The dynamical timescale is obtained to be (the pressure scale height/local sound speed =  $5.17 \times 10^7$  cm/ $1.32 \times 10^8$  cm  $\text{sec}^{-1}$ ) = 0.39 sec. This timescale is much shorter than the local thermal timescale, which indicates that the thermonuclear runaway occurs nearly in hydrostatic equilibrium. Thus, no shock occurs. If the metallicity  $Z$  were enhanced in the quiescent phase by a mixing with core material, the nuclear burning rate  $\epsilon_{\text{nuc}}$  increases but only by a factor of 4 (Guo et al. 2022). Then, no shock wave is expected in the nuclear burning zone. It should be noted that no internal shocks have been reported in numerical calculations after 1990's opacity revisions.

### 3.3 Degeneracy of the envelope

Figure 5(a) shows the locus of the temperature and density at the bottom of hydrogen-rich envelope in the  $\log \rho_{\text{b}} - \log T_{\text{b}}$  plane for one cycle of a hydrogen shell flash. We indicate several characteristic epochs and their times elapsed from stage B ( $t = 0$ ). In the late accreting stage approaching stage A, the bottom of envelope is degenerated, and the density increases with little increase of temperature. As nuclear burning ignites at stage A,  $T_{\text{b}}$  increases by the



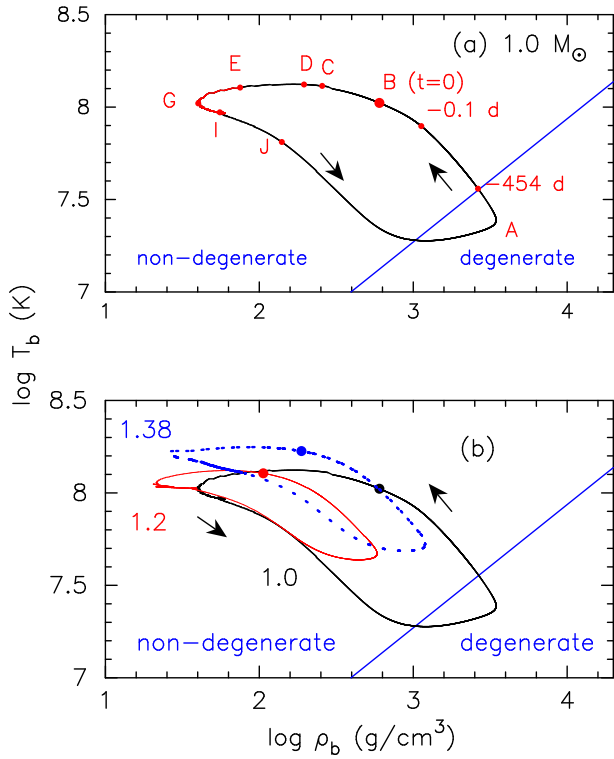


**Fig. 5.** (a) The locus of the temperature and density at the bottom of the hydrogen-rich envelope. Several characteristic stages and their corresponding time (in units of days) are indicated. The blue solid straight line indicates the boundary of degenerate and non-degenerate matter (corresponding to the degeneracy  $\psi = 0$ ). (b) Same as the upper panel but for a comparison with the recurrent nova models of a  $1.2 M_{\odot}$  WD with  $\dot{M}_{\text{acc}} = 2 \times 10^{-7} M_{\odot} \text{ yr}^{-1}$  (thin red line) and a  $1.38 M_{\odot}$  WD with  $\dot{M}_{\text{acc}} = 1.6 \times 10^{-7} M_{\odot} \text{ yr}^{-1}$  (dotted blue line) (Kato et al. 2017a). The filled circles indicate the stage of maximum nuclear burning rate  $L_{\text{nuc}}^{\text{max}}$ , corresponding to stage B in the upper panel.

heating, and  $\rho_b$  decreases by expansion, so that  $(\rho_b, T_b)$  moves upward and the degeneracy is lifted-up before it reaches stage B ( $t = 0$ ), where the nuclear energy generation rate reaches its maximum. As nuclear burning produces a large amount of thermal energy, the temperature quickly increases that makes the envelope expand and the density decrease. When  $(\rho_b, T_b)$  passes point B, the total nuclear burning rate begins to decrease because the density decreases. The thermonuclear flash is stabilized and the envelope settles to a thermal equilibrium state.

Figure 5(b) shows a comparison with two recurrent nova models of a  $1.2 M_{\odot}$  WD having  $\dot{M}_{\text{acc}} = 2 \times 10^{-7} M_{\odot} \text{ yr}^{-1}$  and a  $1.38 M_{\odot}$  WD having  $\dot{M}_{\text{acc}} = 1.6 \times 10^{-7} M_{\odot} \text{ yr}^{-1}$  (Kato et al. 2017a). In such high mass accretion rates, the envelope is hot with large gravitational energy release in the quiescent phase. Thus, the bottom of the envelope is non-degenerate. This is a remarkable contrast to our classical nova model ( $1.0 M_{\odot}$  WD,  $\dot{M}_{\text{acc}} = 5 \times 10^{-9} M_{\odot} \text{ yr}^{-1}$ ).

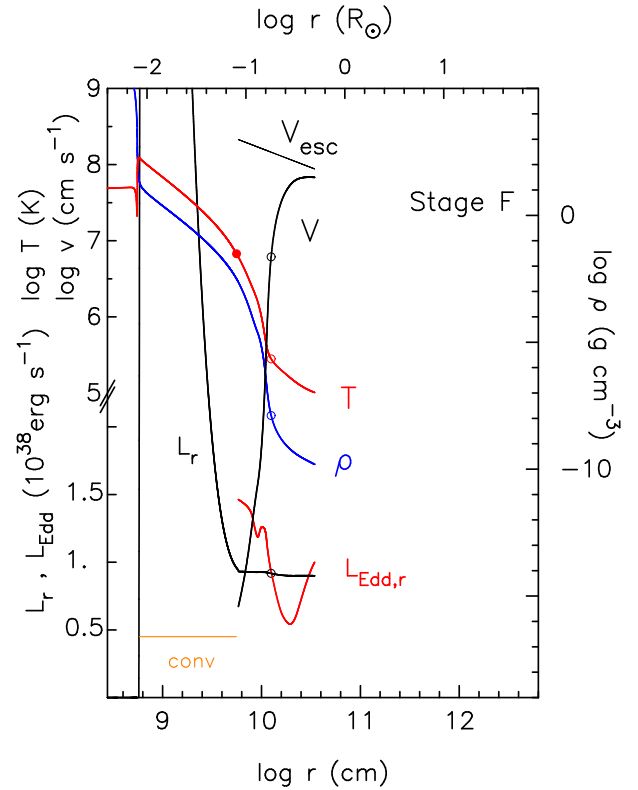


**Fig. 6.** The internal structure at stage F (see Figure 2). The temperature, density, photon flux, velocity, local Eddington luminosity (lower red line), and escape velocity (uppermost black) are shown. The last three are plotted only in the outside of the fitting point. Convective region is denoted by the horizontal orange line. The open circles denote the critical point of the optically thick wind solution (Kato and Hachisu 1994), whereas the filled circle is the fitting point of our wind solution to the internal structure obtained by our Henyey code.

## 4 Evolution of internal structure – expansion and mass loss

### 4.1 Occurrence of optically thick winds

The optically thick wind is accelerated when the photospheric luminosity  $L_{\text{ph}}$  becomes very close to the local Eddington luminosity at the photosphere  $L_{\text{Edd,ph}}$  (Eq.1) (Kato 1985; Kato and Hachisu 2009a). We adopt the surface boundary condition BC1 of Kato and Hachisu (1994). The occurrence condition of winds is satisfied at stage E (see Figure 2), where the mass-loss by optically thick winds begins. The critical point of solar-wind type solution (Bondi 1952; Kato and Hachisu 1994) appears at the photosphere and moves inward in the mass coordinate.

Figure 6 shows the envelope structure at epoch F ( $\log T_{\text{ph}} \text{ (K)} = 5.01$ ), shortly after epoch E (where the wind began). The critical point appears in the wind acceleration region where the velocity (density) quickly increases (decreases). At this stage the wind velocity barely reaches the escape velocity  $v_{\text{esc}} = \sqrt{2GM_{\text{WD}}/r}$ .

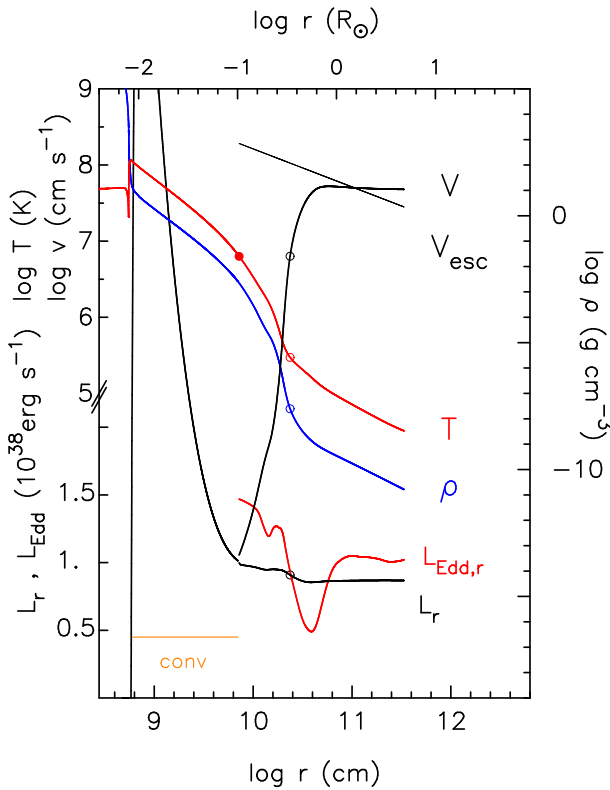


Fig. 7. Same as in figure 6 but at a slightly later stage ( $\log T_{\text{ph}} (\text{K})=4.51$ ).

This figure also shows local luminosity  $L_r$ , the sum of radiative and convective luminosities. It increases in the nuclear burning region and decreases outward being absorbed into the envelope. In the outermost layers,  $L_r$  is almost constant.

We plot the local Eddington luminosity in the radiative region, which is defined as

$$L_{\text{Edd},r} \equiv \frac{4\pi c G M_{\text{WD}}}{\kappa}. \quad (2)$$

The local Eddington luminosity is inversely proportional to the opacity that is a function of the temperature and density. A small dip at  $\log r (\text{cm}) \sim 9.9$  corresponds to a small peak in the opacity contributed by ionized O and Ne ( $\log T (\text{K}) \sim 6.2\text{--}6.3$ ), and a large dip at  $\log r (\text{cm}) \sim 10.3$  is caused by a large Fe peak at  $\log T (\text{K}) \sim 5.2$  (see figure 6 in Kato et al. (2016)). The wind is accelerated where the opacity increases outward and  $L_r$  exceeds the local Eddington luminosity  $L_{\text{Edd},r}$ .

Figure 7 shows the structure at a more expanded stage at  $\log T_{\text{ph}} (\text{K})=4.51$ . The velocity reaches a constant value deep inside the photosphere and exceeds the escape velocity slightly below the photosphere. A strong acceleration occurs around the critical point at  $\log T (\text{K})=5.47$  where the opacity increases outward and the local Eddington luminosity quickly decreases. Note that the photospheric lu-

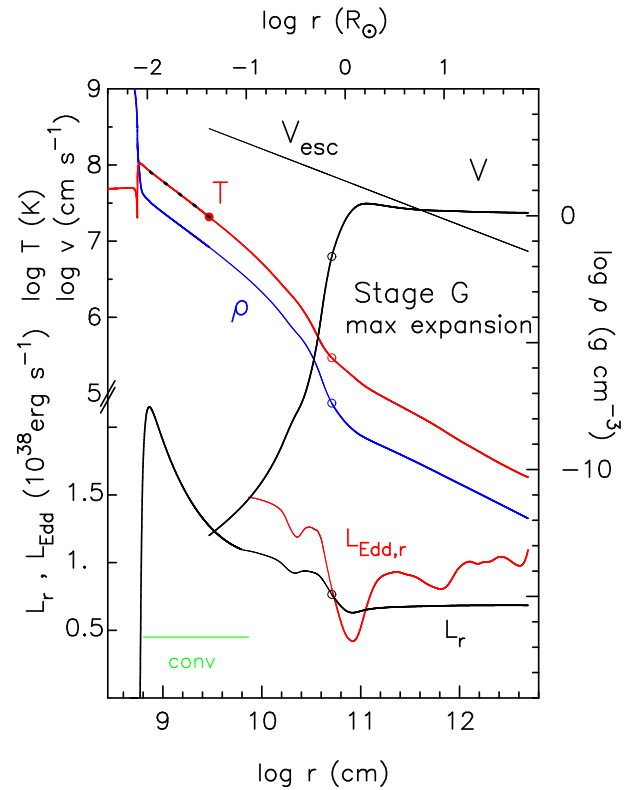


Fig. 8. Internal structure of the envelope at the maximum expansion of the photosphere, stage G. The temperature profile of steady state solution is additionally indicated beyond leftside of the fitting point (dotted black line), that is overlapped with the Henyey solution.

minosity  $L_{\text{ph}}$  does not exceed the photospheric Eddington luminosity  $L_{\text{Edd},\text{ph}}$  whereas the local Eddington luminosity has a dip caused by the Fe-opacity peak around  $\log r (\text{cm}) \sim 10.6$ .

#### 4.2 Maximum expansion of photosphere (stage G)

Figure 8 shows the distribution of the temperature, density, velocity and energy flux at stage G. The temperature and density decreases as  $\rho \propto T^3$ . The radiation pressure is much larger than the gas pressure as  $1 - \beta \sim 0.8$  and  $\gtrsim 0.9$  below and above the critical point, respectively, where  $\beta \equiv P_{\text{gas}}/P_{\text{total}}$  is the ratio of the gas pressure to the total pressure. The velocity quickly increases outward where the local Eddington luminosity decreases corresponding to the Fe peak in the opacity (at  $\log T (\text{K}) \sim 5.2$ ) and the velocity reaches the terminal velocity deep inside the photosphere. The local luminosity  $L_r$  decreases outward in the envelope below the critical point. This is because the photon energy is consumed partly to lift the envelope matter up against the gravity (gravitational energy), to heat the envelope (thermal energy), and to increase the kinetic energy of the winds (see figure 13 below).

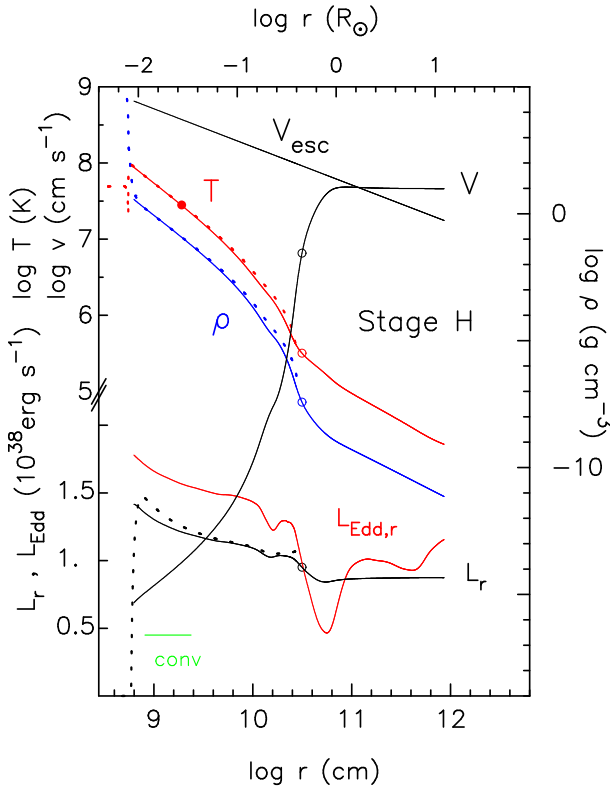


Fig. 9. Same as in figure 6 but for stage H.

The fitting point is indicated by a filled circle on the temperature line (filled red point in figure 8). A dotted line in this figure shows the inward extension of the steady-state wind solution, which agrees well with the temperature variation in the evolution model. This good agreement shows that the envelope has settled to steady state in the almost whole envelope close to the nuclear burning region.

### 4.3 Decay phase

After stage G the photospheric temperature (radius) rises (decreases) with time. The wind mass loss rate turns to decrease (figure 1). The mass of the hydrogen-rich envelope decreases owing mainly to wind mass loss and secondarily to nuclear burning. Figures 9 and 10 show the internal structures at stage H and stage I (wind stopping), respectively. Both the figures show the inner Henyey code solution (dotted line parts) and the steady-state wind solution (solid line parts). The fitting point between the two solutions is indicated by a filled circle on the temperature line. In the leftside to the fitting point we adopt the Henyey code solution, while the steady state wind solution in the exterior to the fitting point. In the both sides the dotted line is very close to the solid line because the envelope has settled to steady state. In stage I, throughout the envelope

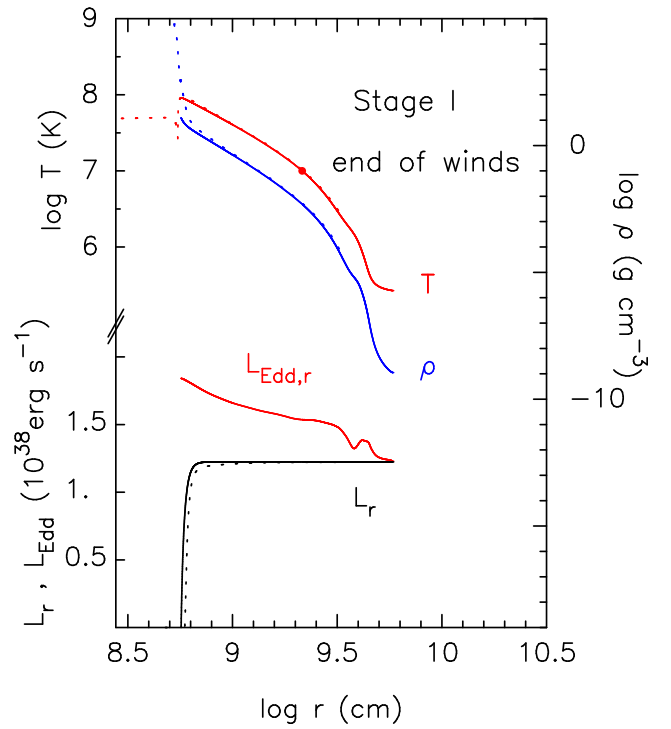


Fig. 10. Same as in figure 6 but for stage I. The optically thick winds have just stopped.

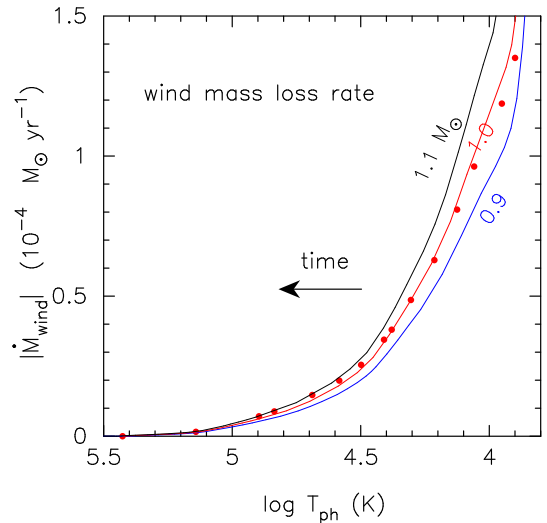


Fig. 11. The wind mass loss rate vs photospheric temperature. The dots indicate those of the present work (optically thick wind solutions). The solid lines are the mass loss rates obtained by Kato and Hachisu (1994) for three WD masses of  $1.1 M_{\odot}$  (black line),  $1.0 M_{\odot}$  (red line), and  $0.9 M_{\odot}$  (blue line) with solar composition.

is in hydrostatic because the wind has just stopped. The structure is very close to that of the hydrostatic (Henyey code) solution. In this way, the envelope evolves almost keeping steady state structure in the wind phase.

Figure 11 shows the mass loss rates after the optical peak obtained in this work in the  $T_{\text{ph}} - \dot{M}_{\text{wind}}$  diagram.



The right-top dot corresponds to stage G and the left-bottom dot to stage I ( $\dot{M}_{\text{wind}} = 0$ ). The mass loss rate decreases as  $T_{\text{ph}}$  increases with time (see figure 1 for the time dependence). The solid lines show the wind mass loss rates in the steady-state sequence (Kato and Hachisu 1994). Our evolution model (dots) shows good agreement with the  $1.0 M_{\odot}$  line. This will be discussed in Section 7.1.

#### 4.4 Envelope expansion and wind mass loss

Figure 12 shows the temporal change of the density distribution. Before the outburst (stage A), the envelope is in plane parallel structure where the density steeply decreases outward. After the shell flash starts the convection widely extends above the nuclear burning zone. In the early phase, such as stage D, the density slowly decreases outward in the convective region, keeping a steep gradient in the radiative region. This means that the envelope expansion in this early stage occurs in the convective region. The convection carries thermal energy upward. As a result, the whole convective envelope is heated up and expands.

After stage E the envelope expands faster in the outer region. The photospheric temperature decreases enough for the opacity to increase outward. Then the radiation pressure gradient increases. If the gradient is large enough for the outer region of envelope to be accelerated to supersonic and eventually to the escape velocity, such matter leaves as the optically thick winds. In the outer region above the critical point, the density decreases as  $\rho \propto r^{-2}$  because of the steady state condition  $4\pi r^2 \rho v = \text{constant}$  with a constant velocity (see figures 7 to 9). To summarize, the envelope starts its expansion first in the convective region, followed by the entire envelope expansion, but especially in the outer radiative region. The transition from the subsonic expansion to radiative-driven supersonic wind is smooth.

Panel (b) in Figure 12 shows the decay phase. Convection still exists at stages G and H, but disappears after stage H. The photospheric radius shrinks with time because the density in the outer envelope decreases. After stage I, the wind has stopped. The envelope further shrinks as the envelope mass decreases owing to nuclear burning, and eventually becomes geometrically thin. At stage J the structure is in plane parallel.

## 5 Energy budget

In this section we discuss how much amount of nuclear energy is consumed to drive the wind mass-loss.

### 5.1 Energy emitted from the photosphere

First of all, we consider a simplest case in which no mass loss occurs during the outburst. Before the onset of thermonuclear runaway, the envelope is cold and geometrically thin. When a shell flash begins the envelope becomes hot and then expands. Thus, the generated nuclear energy is converted to (1) thermal energy to heat the envelope matter, (2) gravitational energy to expand the envelope against the gravity, and (3) radiative energy that is emitted from the photosphere, (4) kinetic energy of expanding matter. Also some of the nuclear energy may flow inward to (5) heat the WD interior, but this inward flow is negligibly small because we adopt such a warm WD model that the WD is in heat balance with the long-term accretion. Thus, the net flux into the WD interior is almost zero (see discussion in Kato et al. (2017b)).

After the envelope expands to the maximum size, the envelope begins to shrink. The gravitational energy is converted to thermal energy, and eventually emitted from the photosphere. The envelope becomes cool and geometrically thin. In short, the produced nuclear energy are all emitted from the photosphere i.e.,  $\int L_{\text{nuc}} dt = \int L_{\text{ph}} dt$ .

### 5.2 Nuclear energy lost in the winds

When mass loss occurs, the ejected matter carries energy away from the WD. In the steady state wind the energy conversion is expressed by an integrated form of (Kato and Hachisu 1994)

$$L_r - \dot{M}_{\text{wind}} \left( \frac{v^2}{2} + \omega_{\text{rad}} + \omega_{\text{gas}} - \frac{GM}{r} \right) = \Lambda, \quad (3)$$

where  $\Lambda$  is a constant throughout the envelope (strictly speaking, outside the fitting point) at a given time  $t$ , and  $L_r$  is the local diffusive luminosity. The other terms are the energies carried with the moving matter, that is, the kinetic energy, enthalpy of radiation  $\omega_{\text{rad}}$  (photon energy trapped in the moving matter), enthalpy of gas  $\omega_{\text{gas}}$ , and gravitational energy.

We depict the distribution of each energy advected by winds and radiative luminosity at the stage of maximum expansion (stage G) in figure 13. In the deep interior of envelope the advection of radiation energy (enthalpy of radiation) is dominant, which decreases outward because it is used to lift up the envelope matter against the gravity. Thus, the both energies (enthalpy of radiation and gravitational energy) are compensated with each other. As a result, the diffusive luminosity  $L_r / \dot{M}_{\text{wind}}$  is dominant near the photosphere.

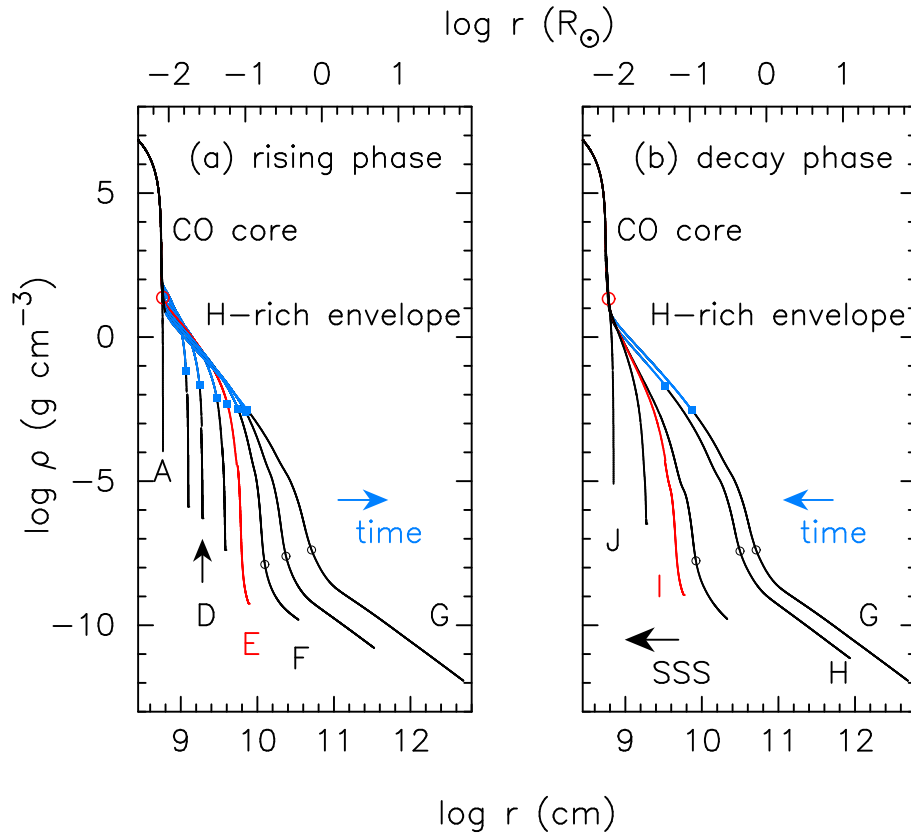


**Fig. 12.** Temporal change in the density distribution: (a) in the rising phase from stage A to stage G, (b) in the decay phase from stage G to stage J. The designated stages are indicated under the lines. The convective region of each stage is plotted in blue except stage E, and the filled blue squares indicate their outer edges, i.e., the border between the convective and radiative regions. The wind occurs at stage E and stops at stage I, both of which are indicated by the red lines. The critical points of the wind solutions are indicated by the small open black circles. The large open red circles show the places of maximum energy generation rate of nuclear burning  $\epsilon_{\text{nuc}}^{\text{max}}$ , for stages E and I, which is close to but slightly above the bottom of the H-rich envelope.

**Table 3.** Energy budget

subject	$E_{\text{nuc}}$	$M_{\text{ej}}$	$E_{\text{rad}}$	$E_{\text{G}}$	$E_{\text{kin}}$
unit	(erg)	( $M_{\odot}$ )	(erg)	(erg)	(erg)
	$3.2 \times 10^{46}$	$3.0 \times 10^{-5}$	$2.1 \times 10^{46}$	$1.1 \times 10^{46}$	$7.3 \times 10^{43}$
%	100	–	64	35	0.23

### 5.3 Energy budget throughout the outburst

The nuclear energy released during the outburst is calculated to be  $E_{\text{nuc}} = \int L_{\text{nuc}} dt = 3.2 \times 10^{46}$  erg from the beginning of the outburst until the epoch of accretion restart. The energy radiated from the photosphere in the same period is  $E_{\text{ph}} = \int L_{\text{ph}} dt = 2.06 \times 10^{46}$  erg. This corresponds to 64 % of the total nuclear energy generation. The rest of the energy is lost in the winds, mainly in the gravitational energy of ejecta  $E_{\text{G}} = \int GM_{\text{WD}} \dot{M}_{\text{wind}} / R_0 dt = 1.1 \times 10^{46}$  erg (35 %), here  $R_0 = 9.95 \times 10^{-3} R_{\odot}$  is the radius originally located before the outburst. The kinetic energy of the ejecta is small  $E_{\text{kin}} = \int (1/2) \dot{M}_{\text{wind}} v^2 dt = 7.3 \times 10^{43}$  erg, corresponding only to 0.23 % of the nuclear energy. These values are summarized in Table 3.

### 6 UV Flash and X-ray flash

After a thermonuclear runaway sets in, the WD immediately brightens up and its luminosity approaches the Eddington luminosity. The photospheric temperature is as high as to emit far UV flux. We plot the multiwavelength light curves for the first few days in figure 14, that is, supersoft X-ray (0.3 – 1.0 keV: 12.4 – 42.3 Å), far UV (100 – 300 Å), and UV (1120 – 2640 Å for the Swift uvw2 band), assuming black body emission. In the first day, the WD is very bright in the 100 – 300 Å band, but much fainter in the other bands. In the following days, these fluxes may be substantially reduced because the optically thick winds start at stage E and may absorb high energy photons. Thus, the nova is very bright in the 100 – 300 Å band only in the first day but may soon become fainter.

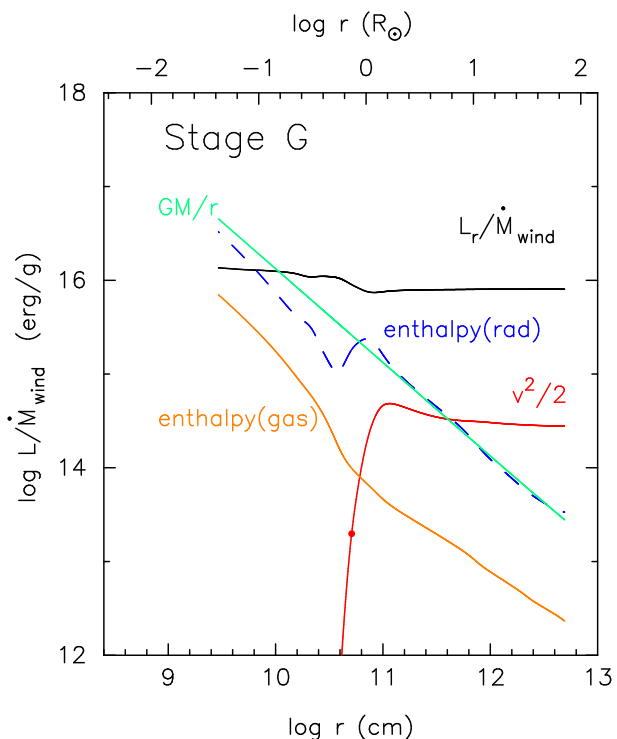


**Fig. 13.** The distribution of the diffusive radiative luminosity per unit mass,  $L_r/\dot{M}_{\text{wind}}$ , and energy advected by winds at the maximum expansion of the photosphere (stage G): gravitational energy  $GM/r$ , radiation enthalpy (rad), gas enthalpy (gas), and kinetic energy  $v^2/2$ . The filled circle on the kinetic energy denotes the critical point. The structure is plotted only for the region outside to the fitting point, i.e., the steady-state wind part of envelope.

This is the far-UV flash. In our model, it occurs 25 d before the optical peak. Our calculation, however, does not include the effects of pre/post-outburst mixing between the WD interior matter and the accreted matter. If an effective mixing occurs, it increases the amount of heavy elements and the evolution timescale may be changed. This mixing effect is discussed in subsection 7.2.

The flux of each band strongly depends on the WD mass. In more massive WDs the temperature  $T_{\text{ph}}^{\text{max}}$  is higher so that the X-ray flux is stronger and the 100–300 Å band flux is relatively weaker. The X-ray flash light curve is presented by Kato et al. (2016) for  $M_{\text{WD}} \geq 1.35 M_{\odot}$  and by Kato et al. (2017a) for  $M_{\text{WD}} = 1.2 M_{\odot}$  and  $1.38 M_{\odot}$ . For  $M_{\text{WD}} = 1.38 M_{\odot}$  the X-ray flash lasts about 1 day and is as bright as  $\log(L_X/L_{\odot}) \sim 4.4$  because the temperature  $\log T_{\text{ph}}^{\text{max}}$  (K)  $\sim 6.1$  is much higher than that of the  $1.0 M_{\odot}$  WD.

Morii et al. (2016) and Kato et al. (2016) attempted to detect such early X-ray flushes, but not detected.<sup>1</sup> Cao et al. (2012) presented multiwavelength light curves of 29

<sup>1</sup> König et al. (2022) reported an X-ray flash in the classical nova YZ Ret on 2020 June 26 with the eROSITA instrument on board Spectrum-Roentgen-Gamma (STG). This is the first detection of X-ray flash in novae.

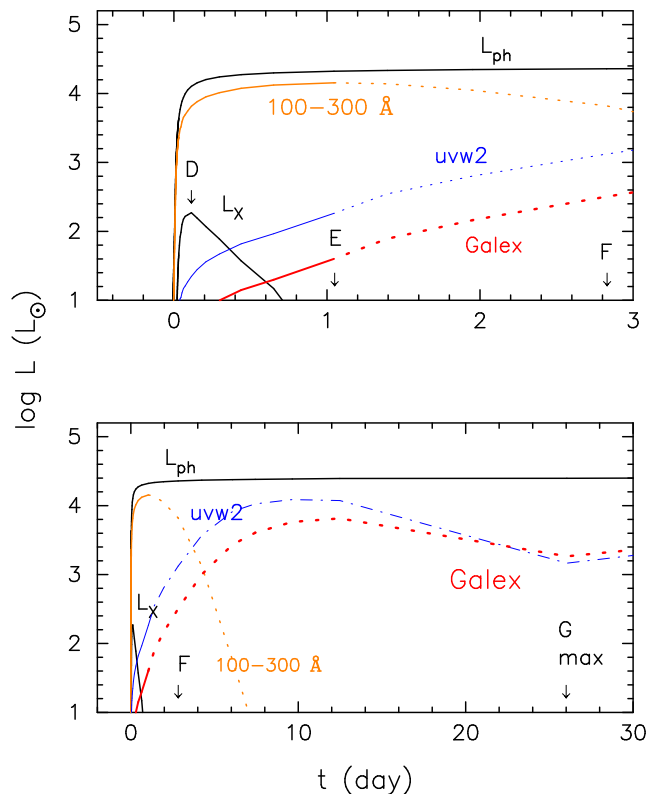


**Fig. 14.** The photospheric bolometric luminosity,  $L_{\text{ph}}$  (upper black line in each panel), luminosities of the supersoft X-ray  $L_X$  (0.3–1.0 keV: lower black line), 100–300 Å band (orange line), uvw2 (1120–2640 Å) band (blue line), and the Galex UV (1786–2846 Å) band (red line). The upper panel shows the light curves for the first three days of the outburst, while lower shows the first 30 days. The stages D, E, F, and G are indicated. The supersoft X-ray luminosity reaches its maximum at stage D. The wind mass loss starts at stage E, so these high energy fluxes of the supersoft X-ray, 100–300 Å, uvw2, Galex UV bands could be partly self-absorbed by the wind itself. Stage G corresponds to the stage of the maximum wind mass-loss rate and possibly the optical peak.

novae in M31. Their light curves include optical, IR, and GALEX UV (Galaxy Evolution Explorer satellite: effective wavelength 2316 Å with the band width of 1060 Å) bands. They detected UV fluxes in few novae prior to the apparent optical maximum. For comparison, we plot the theoretical UV light curve in Figure 14, calculated from the blackbody luminosity between 740 Å and 1703 Å.

## 7 Discussion

### 7.1 Comparison with steady state sequence model

Prialnik et al. (1986) calculated one cycle of nova outburst on a  $1.25 M_{\odot}$  WD and showed that the envelope structure at  $t = 10^6$  sec is quite close to steady state over a wide region, from the inside to the critical point ( $r_{\text{cr}} = 3.4 R_{\odot}$ ) to the outside of the photosphere ( $r_{\text{ph}} = 36 R_{\odot}$ ). Kato (1983) proposed a new way to follow the decay phase of

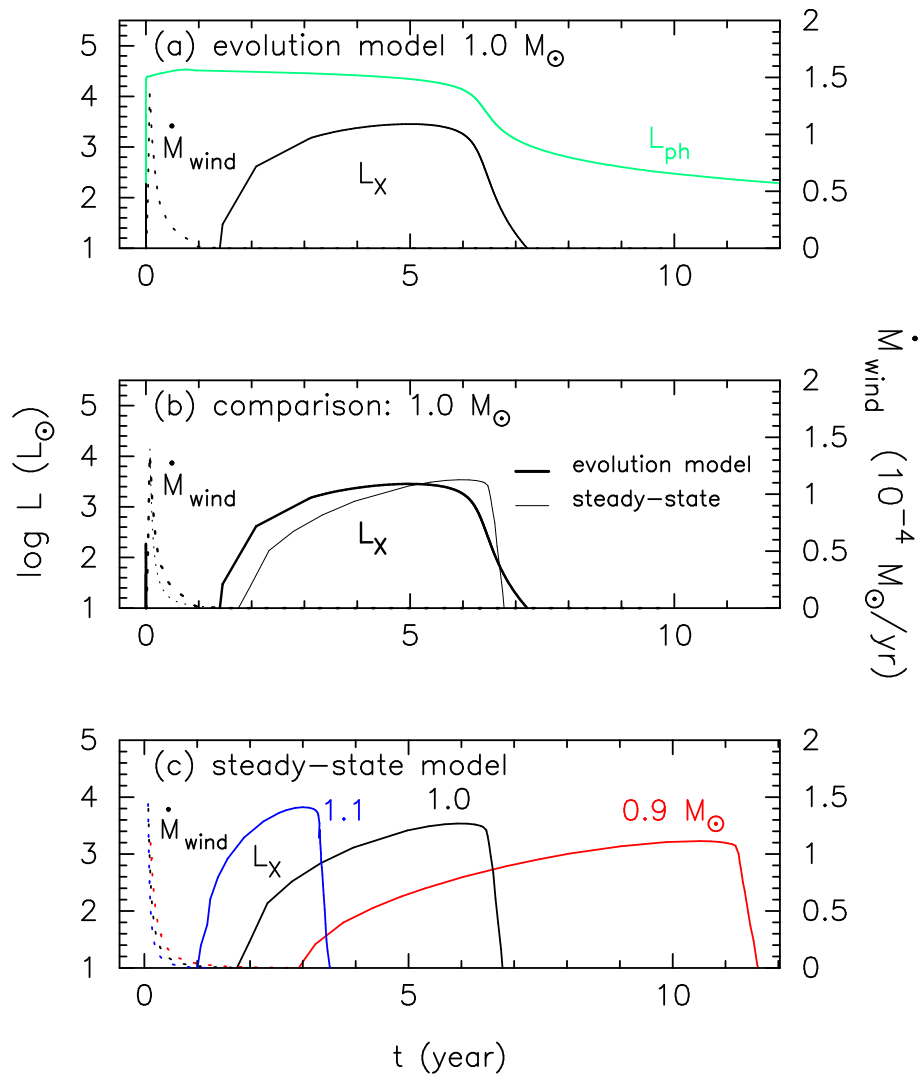


**Fig. 15.** Comparison of the X-ray light curves  $L_X$  (0.3 – 1.0 keV) between our evolution model and steady state sequence. (a) Evolution model of our  $1.0 M_{\odot}$  WD. The green line shows the photospheric luminosity ( $L_{\text{ph}}$ ), whereas the solid black line is the X-ray light curve ( $L_X$ , scale on the left-side ordinate). The X-ray flux is prominent in the X-ray flash ( $t \sim 0$ ) and SSS phase (from  $\sim 2$  yr to  $\sim 6$  yr). The dotted black line indicates the wind mass loss rate with the scale on the right-side ordinate. (b) Comparison of our evolution model (in panel (a)) with the steady-state decay phase model of  $1.0 M_{\odot}$  (thin lines). The origin of the steady-state model is set at the peak of the wind mass loss in the evolution model. (c) Three steady state sequence models of  $0.9 M_{\odot}$  (red line),  $1.0 M_{\odot}$  (black), and  $1.1 M_{\odot}$  (blue) WDs with the solar abundance (Kato and Hachisu 1994). The  $1.0 M_{\odot}$  WD model is the same as that in panel (b).

nova outbursts with the sequence of steady-state solutions of decreasing envelope mass. This model is based on the assumption that the envelope has been settled down to steady state after the optical peak.

In 1990's the opacity tables are revised. The new opacities (OPAL or OP: Seaton et al. (1994)) has a prominent peak at  $\log T$  (K)  $\sim 5.2$  owing to Fe ionization, even for the solar abundance. This large peak causes strong acceleration of winds and envelope structure during an extended phase has been drastically changed (Kato and Hachisu 1994). The evolution calculation becomes much difficult, and thus, each group has adopted each mass loss scheme to avoid the opacity peak and to accomplish their calculation until the end of a flash. In such treatments the photospheric temperature hardly decreases much below  $\log T$  (K)  $\sim 5.2$ , so it is difficult to calculate theoretical light curves to be compared with actual novae of which temperature typically decreases to  $T_{\text{eff}} < 10,000$  K (e.g., V339 Del:  $T_{\text{ph}} \lesssim 10,000$  and  $R > 100 R_{\odot}$  Skopal et al. (2014)).

Now, the optically thick wind theory is only the way to properly calculate nova light curves, at least, in the wind phase. Until now we have presented two different ways for calculating nova light curves based on the optically thick wind theory, that is, (i) quasi-evolution sequence of steady state solutions, assuming the entire envelope is in steady state (Kato and Hachisu 1994), and (ii) evolution calculation with Henyey code, in which steady state solutions are incorporated in the wind phase (this work).

The first method (i) has been studied and applied to a number of novae. Kato and Hachisu have systematically calculated steady state sequences with various parameters for classical novae and have fitted observational properties of various types of novae (Hachisu and Kato 2006; Hachisu and Kato 2007; Hachisu et al. 2008; Hachisu and Kato 2010; Hachisu and Kato 2014; Hachisu and Kato 2015; Hachisu and Kato 2016a; Hachisu and Kato 2016b; Kato et al. 2009b; Kato et al. 2021; Kato et al. 2020).

The second way (ii) is the one we took the present work. This is the first accurate time-dependent calculation for classical novae, so that we have a chance to compare these two ((i) and (ii)) evolution sequences. The treatment (i) is less accurate because it lacks some time-dependent terms, but the calculation is much easier than that of (ii). We already confirmed in section 4 that the internal structure of the envelope is close to that of the steady state solution in the decay phase. In what follows we compare the evolution timescale of these two nova models.

Figure 15(a) shows our evolution model (i). The solid lines denote the bolometric luminosity  $L_{\text{ph}}$  and the super-soft X-ray flux  $L_{\text{X}}$ . The X-ray flash is shown at  $t \sim 0$  yr and the SSS (supersoft X-ray source) phase emerges from  $t \sim 2$

yr to  $\sim 6$  yr. We plot the wind mass loss rate (dotted line) instead of the optical magnitude because the optical flux in most novae are dominated by free-free emission which is closely related to the wind mass loss rate.

Figure 15(b) compares our evolution model (thick line) with a steady-state sequence model (thin line) for a  $1.0 M_{\odot}$  WD with the solar composition ( $X = 0.7$ ,  $Y = 0.28$ , and  $Z = 0.02$ ) (Kato and Hachisu 1994). The steady state sequence model begins at  $t = 26$  day  $= 0.07$  yr, to fit stage G in the evolution model.

Despite the difference between the two methods ((i) and (ii)), the two X-ray light curves are in good agreement, in the main characteristic properties, i.e., the decay of wind mass loss rate, X-ray turn-on time, peak X-ray flux, and X-ray turn-off time. The main difference between the two models is the gravitational energy release  $L_{\text{G}}$ . In the steady state model (i),  $L_{\text{G}}$  is partly included in the wind phase, but not included in the SSS phase. The resemblance of two different light curves is mainly due to small contribution of  $L_{\text{G}}$  in the evolution model (ii), which is a twentieth of  $L_{\text{ph}}$  in the SSS phase as shown in figure 3.

The X-ray turn-off time and SSS duration are good indicators of the WD mass and have been used to estimate the WD mass of individual novae. To see the dependence of a SSS phase on the WD mass, we plot panel (c) in Figure 15 for three steady state sequence models of different WD masses, i.e.,  $0.9 M_{\odot}$ ,  $1.0 M_{\odot}$ , and  $1.1 M_{\odot}$  (Kato and Hachisu 1994). The light curves of the  $0.9$  and  $1.1 M_{\odot}$  show much different timescales and peak fluxes. We may safely use the results of steady state sequence models (i) to estimate the WD mass.

Whereas the Henyey code model (ii) needs a complicated process and many manual iteration to calculate one cycle of a nova outburst, calculation with steady state (wind/no wind) sequence (i) is relatively easier. In this sense the steady state sequence (i) is a good way to calculate the decay phase of a nova outburst.

## 7.2 Effects of CO enrichment

During a nova outburst nuclear burning converts hydrogen to helium but the total amount of heavy elements is unchanged. In our  $1.0 M_{\odot}$  model the chemical composition of ejecta changes from  $X = 0.7$ ,  $Y = 0.28$ , and  $Z = 0.02$  (accreted matter) to  $X = 0.65$ ,  $Y = 0.33$ , and  $Z = 0.02$  (ejecta in the decay phase). On the contrary, classical nova spectra show enhancements of heavy elements such as C, N, O, Ne, or Mg (see, e.g., Hachisu and Kato (2010) for a summary), which are considered to originate from WD interiors.

In spherically symmetric (1D) calculations such as ours, the convection does not reach down to the CO core below the interface of the accreted hydrogen-rich matter, which prevents CO-rich matter from entering into the hydrogen-rich envelope. We did not include particular mixing mechanisms of dredging up WD core material into envelope to avoid free parameters such as an uncertain mixing degree. Also, we did not include diffusion processes of nuclei in the quiescent phase. The timescale of diffusion is estimated to be  $3.6 \times 10^4$  yr, using Equation (A3) in Shen et al. (2009), for hydrogen atoms to diffuse from the bottom of hydrogen-rich envelope ( $X = 0.1$ ) down to the top of He layer ( $X = 0.0003$ ). This timescale is much longer than the accreting phase of 5358 yr, so the diffusion process is not efficient.

Effects of CO enhancement on nova outbursts has been studied by Sala & Hernanz (2005); Denissenkov et al. (2013); Chen et al. (2019); Starrfield et al. (2020). Denissenkov et al. (2013) and Chen et al. (2019) reported that nova outbursts with CO enhancements in the accreted matter shows a smaller ignition mass, lower maximum temperature  $T^{\text{max}}$  at the shell flash, and less extent of excursion toward the lower temperature in the H-R diagram. From these calculations we see two opposite effects of CO enrichment. A larger CO content enhances the nuclear burning, which would increase the expansion rate of the burning shell and shorten the timescale of a flash, that is, the X-ray flash phase would become shorter and the wind mass loss would start earlier, if the other parameters are the same. On the other hand, the flash will be weaker for a smaller ignition mass, which would increase the timescale of a flash. These two effects work in the opposite direction, and it is not clear, at present, which effect is more important in the early phase of a nova outburst.

For the decay phase, on the other hand, the effects of heavy element content have been systematically studied with the steady state sequence models (Kato 1997; Hachisu and Kato 2006; Hachisu and Kato 2010; Hachisu and Kato 2015; Hachisu and Kato 2016a; Kato et al. 2021). For a larger  $Z$  both the wind mass loss rate and velocity increase. The light curves decay faster after the optical maximum, and the following supersoft X-ray source phase becomes shorter. Hachisu and Kato (2006) obtained the wind durations  $t_{\text{wind}} = 218$  days for CO nova 2 (CO2) chemical composition ( $X = 0.35$ ,  $Y = 0.33$ ,  $X_{\text{CNO}} = 0.30$ , and  $Z = 0.02$ ) and  $t_{\text{wind}} = 712$  days for solar ( $X = 0.70$ ,  $Y = 0.28$ , and  $Z = 0.02$ ), where the WD mass is  $1.0 M_{\odot}$ . The timescale of CO2 composition is about 3 times shorter than that of solar.

In our present  $1.0 M_{\odot}$  model the time from the start of ignition to the maximum expansion of the photosphere is

about 26 days (see Table 2). On the other hand, a typical timescale from the ignition to the maximum brightness is estimated as from a few to several days (e.g., 3 days in V339 Del, see Schaefer et al. (2014) and Skopal et al. (2014)). The difference may come from the difference of physical parameters such as abundance and mass accretion rate.

### 7.3 Comparison with Hillman et al. (2014)

Theoretical light curves of classical nova outbursts have rarely been published because of the difficulties in calculating a full cycle of a classical nova evolution. Hillman et al. (2014) presented photospheric temperature variations and multiwavelength light curves based on the hydrogen shell flash models obtained by Prialnik and Kovetz (1995) and Yaron et al. (2005). In this subsection we compare our  $1.0 M_{\odot}$  classical nova model with Hillman et al.'s 100.10.8 model ( $M_{\text{WD}} = 1M_{\odot}$ ,  $T_{\text{c}} = 10^7 \text{K}$ ,  $\dot{M}_{\text{acc}} = 10^{-8} M_{\odot} \text{yr}^{-1}$ ).

#### 7.3.1 Photospheric temperature

Figure 16(a) shows the photospheric temperature  $T_{\text{ph}}$  variation of our model as a function of time. The wind phase is the period between stage E and stage I, and the SSS phase is between stage I and stage J. To compare Hillman et al.'s temperature profile, we adopt a logarithmic time for the abscissa of panel (b), in which the origin of time is shifted by 4.93 days.

After the ignition of a thermonuclear runaway,  $T_{\text{ph}}$  quickly reaches maximum (stage D). Then  $T_{\text{ph}}$  decreases as the envelope expands, and takes a minimum value in a few days. After the maximum expansion of the photosphere ( $T_{\text{ph}}$  minimum),  $R_{\text{ph}}$  begins to contract with the photospheric temperature being increased as the mass of hydrogen-rich envelope decreases mainly by wind mass loss. When  $T_{\text{ph}}$  increases to  $\sim 3 \times 10^5$  K, the nova enters a supersoft X-ray source (SSS) phase.

Figure 16(b) and (c) show photospheric/effective temperature variations in a logarithmic time of ours and Hillman et al.'s, respectively. Although the amplitude of photospheric temperature variation of our model is comparable with that of Hillman et al., panel (b) shows a smooth decrease/increase in the cool (expanded) phase while panel (c) displays the sudden changes. The variation of photospheric temperature in the expanded phase is correlated with wind mass-loss rates (see Figure 11). Such a sudden decrease/increase of  $T_{\text{eff}}$  should accompany some drastic change in the envelope, but no description is given in Prialnik and Kovetz (1995), Hillman et al. (2014), and Yaron et al. (2005).

Observationally gradual temperature increases are re-



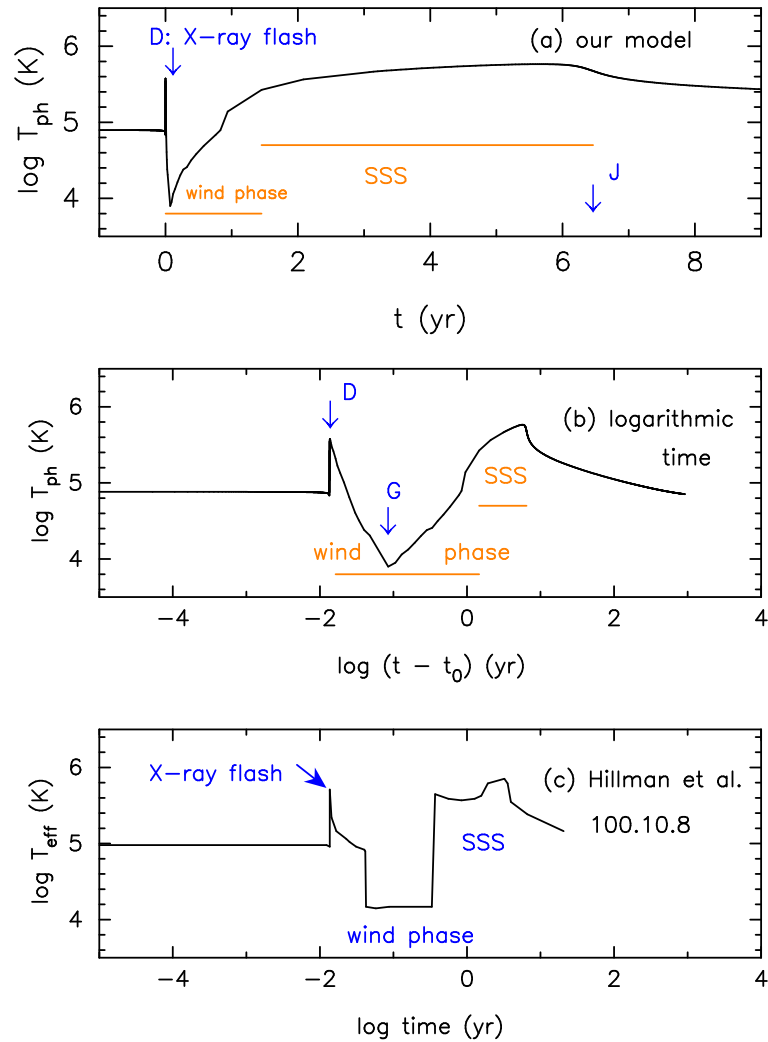


**Fig. 16.** Comparison of the temperature evolution of our model with Hillman et al. (2014)’s model. (a) Our photospheric temperature is plotted against time, where  $t = 0$  is the time at  $L_{\text{nuc}}^{\text{max}}$ . (b) The same quantity as in panel (a) is plotted as a function of a logarithmic time, in which the origin of time is shifted by 4.93 days before stage B to make comparison with panel (c) easier. (c) The temporal change of  $T_{\text{eff}}$  in model 100.10.8 ( $1 M_{\odot}$ ,  $T_c = 10^7$  K,  $\dot{M}_{\text{acc}} = 10^{-8} M_{\odot} \text{yr}^{-1}$ ) of Hillman et al. (2014).

ported after the optical maximum (Cassatella et al. (2002); Cassatella et al. (2004); Kato et al. (2009b)). These smooth temperature increases are consistent with our model.

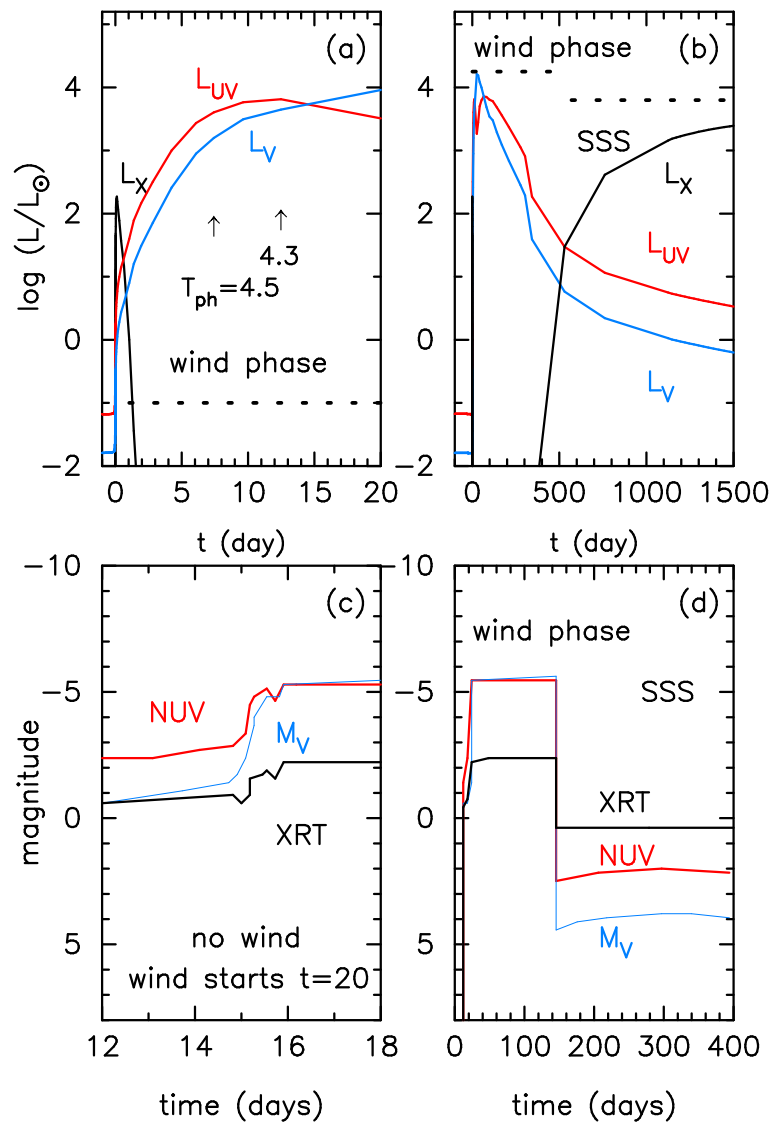
### 7.3.2 Multiwavelength light curves

Figure 17(a) and (b) show our light curves of three wavelength bands, i.e., supersoft X-ray, Galex UV, and  $V$  calculated from  $T_{\text{ph}}$  and  $L_{\text{ph}}$  assuming blackbody. Panel (a) shows the first 20 days, whereas panel (b) covers 1500 days. Note that the blackbody  $V$  light curve  $L_V$  does not accurately correspond to the observed ones because the emission in classical novae is dominated by free-free emission not by blackbody emission (see, e.g., Figure 4 in Kato et al. (2017) for the comparison of the light curves of free-free emission and blackbody). In the early phase (in panel

(a)) the brightest emission band shifts from X-ray to UV toward the optical peak ( $t = 26$  day). In the decay phase (panel (b)), it shifts from optical, UV to X-ray.

The lower two panels show light curves in magnitudes, obtained by Hillman et al. (2014) for visual ( $M_V$ ), GALEX NUV, and soft X-ray (Swift XRT), which are reproduced from their figure 4 (panel 2). We did not find any definitions on their origin of time and X-ray magnitude.

Hillman et al.’s light curves show sudden changes, which are related with the nearly discontinuous temperature decrease to and rise from the minimum  $\log T_{\text{eff}}(\text{K}) \approx 4.2$  as seen in Figure 16(c). These variations are stark contrast to the smooth changes of our luminosity and temperature curves in panels (a) and (b). Our supersoft X-ray light curve shows a precursor flash 26 days before the  $V$  maximum while a much stronger precursor flash occurs in a far



**Fig. 17.** Comparison of light curves between our model and Hillman et al.'s model. The upper two panels show three wavelength bands in V, UV and X-rays in 20 days (a) and 1500 days (b). The wind phase and SSS phase are indicated by the dotted horizontal lines. In panel (b) the X-ray flash is overlapped to the other two lines at  $t$  (day)  $\sim 0$ . The lower two panels show the model 100.10.8 ( $1M_{\odot}$ ,  $T_c = 10^7\text{K}$ ,  $\dot{M}_{\text{acc}} = 10^{-8}$ ,  $M_{\odot} \text{ yr}^{-1}$ ) of Hillman et al. (2014).

UV range of  $100 - 300 \text{ \AA}$  (figure 14).

Hillman et al. (2014) claimed that they theoretically predicted the “UV precursor flashes and pre-maximum halts.” These features are different from our smooth light curves. No X-ray flash exists in panel (d). We strongly encourage the authors to publish internal structures of the envelope and mass loss rates (see discussion and Table 1 in Kato et al. (2017)).

## 8 Conclusions

Our main results are summarized as follows.

1. We calculated self-consistent models for one cycle of a classical nova outburst, in which winds are driven by the

radiation pressure gradients. The model is a  $1.0 M_{\odot}$  WD with a mass accretion rate of  $\dot{M}_{\text{acc}} = 5 \times 10^{-9} M_{\odot} \text{ yr}^{-1}$  (the recurrence period is 5370 years). The wind mass loss rate reaches a peak  $1.4 \times 10^{-4} M_{\odot} \text{ yr}^{-1}$  at the epoch of maximum expansion of the photosphere when the photospheric temperature decreases to  $\log T_{\text{ph}} (\text{K}) = 3.90$ .

2. The nuclear energy generated during the flash is emitted in a form of radiation (64 %), or is converted to the gravitational energy of the ejecta by lifting them up against the gravity (35 %) and to the kinetic energy of the ejecta (0.23 %).

3. The nuclear energy at thermonuclear runaway is once stored as heat energy ( $L_G$ ) and emitted gradually throughout the entire period of the flash. Thus, no internal shocks

or blast waves appear in the envelope. Also, the photospheric luminosity does not exceed the Eddington luminosity at the photosphere.

4. In a very early phase of the outburst the  $1.0 M_{\odot}$  WD is very bright in a far UV band (100 - 300 Å), but not so bright in the supersoft X-ray band (0.3 – 1.0 keV). This UV flash occurs 25 days before the optical peak. It should be noted that these individual characteristic properties depend very much on the WD mass, mass accretion rate, and chemical composition of the envelope.

5. The envelope structure approaches steady state after the maximum expansion of photosphere, mainly because the gravitational energy release  $L_G$  is negligibly small compared with diffusive luminosity  $L_r$ . In such a circumstance (very small  $L_G$ ), the optically thick wind theory (a sequence of steady state wind solutions) is a good approximation to the decay phase of a nova outburst.

6. Hillman et al. (2014)'s three band light curves show a rectangle shape corresponding to the quick change of effective temperature. Our evolution model shows, on the contrary, gradual change in the multiwavelength light curve, corresponding to the gradual change of structure, temperature, and wind mass loss rate.

## Acknowledgments

We are grateful to the anonymous referee for useful comments that improved the manuscript.

## References

- Arai, A., Uemura, M., Kawabata, K. S., et al. 2010, PASJ, 62, 1103
- Aydi, E. et al. 2020, nature astronomy, 4, 776
- Bondi, H. 1952, MNRAS, 112, 195
- Cao, Yi. et al. 2012, ApJ, 752, 133
- Casanova, J., José, J., García-Berro, Calder, A., & Shore, S. N. 2010, A&A, 513, L5
- Cassatella, A., Altamore, A., & González-Riestra, R. 2002, A&A, 384, 1023
- Cassatella, A., Lamers, H. J. G. L. M., Rossi, C., Altamore, A., & González-Riestra, R. 2004, A&A, 420, 571
- Chomiuk, L., Metzger, B. D., Shen, K.J. 2021, ARA&A, 59, 391
- Chen, J-L, et al. MNRAS, 490, 1678
- Denissenkov, P. A., et al. 2013, ApJ, 762, 8
- Drake, J. J. & Orland, S. 2010, ApJL720 L195
- Finzi, A., Wolf, R. A. 1971, A&A, 11, 418
- Friedjung, M. 1966, MNRAS, 132, 317
- Gehrz, R. D., Harrison, T. E., Ney, E. P., et al. 1988, ApJ, 329, 894
- Glasner, X. A, Livne, E., & Truran, W. 2012, A&A, 427, 2411
- Guo, Y., Wu, C., & Wang, B. 2022, A&A, 660, A53
- Hachisu, I., & Kato, M. 2004, ApJ, 612, L57
- Hachisu, I., & Kato, M. 2006, ApJS, 167, 59
- Hachisu, I., & Kato, M. 2007, ApJ, 662, 552
- Hachisu, I., & Kato, M. 2010, ApJ, 709, 680
- Hachisu, I., & Kato, M. 2014, ApJ, 785, 97
- Hachisu, I., & Kato, M. 2015, ApJ, 798, 76
- Hachisu, I., & Kato, M. 2016a, ApJ, 816, 26
- Hachisu, I., & Kato, M. 2016b, ApJS, 223, 21
- Hachisu, I., & Kato, M. 2018a, ApJ, 858, 108
- Hachisu, I., & Kato, M. 2018b, ApJS, 237, 4
- Hachisu, I., & Kato, M. 2019a, ApJS, 241, 4
- Hachisu, I., & Kato, M. 2019b, ApJS, 242, 18
- Hachisu, I., & Kato, M. 2021a, ApJS, 253, 27
- Hachisu, I., Kato, M., & Cassatella, A. 2008, ApJ, 687, 1236
- Hachisu, I., Saio, H., & Kato, M. 2016, ApJ, 824, 22
- Hachisu, I., Saio, H., Kato, M., et al. 2020, ApJ, 902, 91
- H.E.S.S. Collaboration, 2022, Science, 376, 77
- Hillman, Y., Prialnik, D., Kovetz, A., Shara, M. M., & Neill, J. D. 2014, MNRAS, 437, 1962
- Idan, I., Shaviv, N. J., & Shaviv, G. 2013, MNRAS, 433, 2884
- Iben, I. Jr. 1982, ApJ, 259, 244
- Iglesias, C. A., & Rogers, F. J. 1996, ApJ, 464, 943
- José, J., Shore, S. N., & Casanova, J. 2020, A&A, 634, A5
- Kato, M. 1983, PASJ, 35, 507
- Kato, M. 1985, PASJ, 37, 19
- Kato, M. 1997, ApJS, 113, 121
- Kato, M., & Hachisu, I. 1994, ApJ, 437, 802
- Kato, M., & Hachisu, I. 2009a, ApJ, 699, 1293
- Kato, M., & Hachisu, I. 2020, PASJ, 72, 82
- Kato, M., Hachisu, I., & Cassatella, A. 2009b, ApJ, 704, 1676
- Kato, M., Hachisu, I., & Henze, M. 2013, ApJ, 779, 19
- Kato, M., Hachisu, I., & Saio, H. 2017, in Proc. Palermo Workshop on “The Golden Age of Cataclysmic Variables and Related Objects IV.” ed. F. Giovannelli et al. (Trieste: SISSA PoS), 315, 56
- Kato, M., Saio, H., Hachisu, I., et al. 2014, ApJ, 793, 136
- Kato, M., Saio, H., & Hachisu, I. 2015, ApJ, 808, 52
- Kato, M., Saio, H., & Hachisu, I., 2017a, ApJ, 838, 153
- Kato, M., Saio, H., & Hachisu, I., 2017b, ApJ, 844, 143
- Kato, M., Saio, H., & Hachisu, I., 2018, ApJ, 863, 19
- Kato, M., Saio, H., & Hachisu, I., 2020, ApJ, 892, 15
- Kato, M., Saio, H., & Hachisu, I., 2021, PASJ, 73, 1137
- Kato, M., et al. 2016, ApJ, 830, 40
- Kikuchi, S., Mikami, Y., & Kondo, M. 1988, PASJ, 40, 491
- König, O., Wilms, J., Arcodia, R., et al. 2022, Nature, 605, 248,
- Kovetz, A. 1998, ApJ, 495, 401
- Morii, M., Yamaoka, H., Mihara, T., Matsuoka, M., & Kawai, N. 2016, PASJ, 68, S11
- Nariai, K., Nomoto, K., & Sugimoto, D. 1980, PASJ, 32, 473
- Prialnik, D., 1986, ApJ, 310, 222
- Prialnik, D., & Kovetz, A. 1995, ApJ, 445, 789
- Rugles, C. L. N., Bath, G. T., 1979, A&A, 80, 97
- Sala, G., & Hernanz, M. 2005, A&A, 439, 1061
- Schaefer, G. H., Brummelaar, T. T., Gies, D. R., et al. 2014, Nature, 515, 234
- Seaton, M. J., Yan, Y., Mihalas, D., Pradhan, A., K., 1994, MNRAS, 266, 805

- Selvelli, P., & Gilmozzi, R. 2019, *A&A*, 622, A186
- Sion, E. M., Acierno, M.J., & Tomczyk, S. 1979, *ApJ*, 230, 832
- Shen, K.J., Idan, I., & Bildsten, L. 2009, *ApJ*, 705, 693
- Skopal, A. et al. 2014, *A&A*, 569, A112
- Sparks, W. N., Starrfield, S., & Truran J. W. 1978, *ApJ*, 220, 1063
- Starrfield, S., Bose, M., Iliadis, C. et al. (2020) *ApJ*, 895, 70
- Tang, S., Bildsten, L., Wolf, W. M., et al. 2014, *ApJ*, 786, 61
- Townsley, D. M., Bildsten, L. 2004, *ApJ*, 600, 390
- Wolf, W. M., Bildsten, L., Brooks, J., et al. 2013, *ApJ*, 777, 136  
(Erratum: 2014, *ApJ*, 782, 117)
- Yaron, O., Prialnik, D., Shara, M.M., & Kovetz, A. 2005, *ApJ*, 623, 398
- Zytkow, A. 1972, *Acta Astronomy*, 22, 103